

Crystallographically Oriented Hybrid Perovskites via Thermal Vacuum Codeposition

Nadja Klipfel, Cristina Momblona, Hiroyuki Kanda, Naoyuki Shibayama, Yuiga Nakamura, Mounir Driss Mensi, Cheng Liu, Cristina Roldán-Carmona,* and Mohammad Khaja Nazeeruddin*

Hybrid lead halide perovskites typically form polycrystalline films that have multiple grain sizes and surface defects. A key engineering challenge toward commercialization is therefore the production of homogeneous, defect-free large-area devices achieving high efficiency. New market opportunities may arise from vacuum-deposited perovskites if detailed understanding and control of crystal formation are available. Of the many factors that make reproducibility of device performance difficult, two variables are identified that have not yet been considered in detail: deposition speed and underlayer material selection. Herein, it is demonstrated that small changes in the perovskite growth rate ($0.18\text{--}0.72\text{ \AA}\cdot\text{s}^{-1}$) substantially affect the preferred crystal orientation. Further, varying underlayer interfaces greatly influence the composition of the final perovskite and thus its energetic profile. The research aids control in fine-tuning the perovskite film at the nanometer scale, which enables the reproducible fabrication of vertically aligned and micrometer-sized grain features, highly demanded for in high-quality semiconductors.

1. Introduction


Organic–inorganic perovskite materials have emerged as powerful alternatives for low-cost, highly efficient third-generation solar cells. The combination of optimal optoelectronic properties, low processing costs, and high tolerance to crystal defects could overcome current limits on photovoltaic manufacturing by making use of a large variety of solution and vapor-based routes.^[1–6] To date, the leading limitation of perovskite technology is the high instability under heat and light-soaking conditions. Although early studies neglected the effect of crystal defects in highly efficient formulations, recent investigations on trap-mediated decomposition indicate a different scenario in which bulk and surface defects strongly impact long-term stability.^[7–9] This opens the question on the

role of crystallization and processing routes on operational stability, and the possibility to fine-tune the film deposition toward low-defect crystals. Unfortunately, techniques targeting film morphology and orientation to improve stability, without sacrificing efficiency, are still insufficient, and the efficiency records achieved so far use fast depositions via solution-based processing, at laboratory scales.^[10] Consequently, there is a considerable lack in understanding of crystal formation obtained from non-conventional processes, which might become crucial to ensure the production of efficient and stable devices. In this context, thermal coevaporation is a technique with great potential. It allows precise monitoring of a precursor's stoichiometry, film thickness, and crystal growth rate at the nanometer scale via a solvent-free methodology. Vacuum deposition was first used in the perovskite field in 2013 when Liu et al. demonstrated for the first time a planar perovskite solar cell (PSC) of $\text{CH}_3\text{NH}_3\text{PbI}_{3-x}\text{Cl}_x$ deposited on top of a metal oxide layer reaching a power conversion efficiency (PCE) of 15.4%.^[11] In 2014, Roldán-Carmona et al. demonstrated the versatility of the coevaporation method by evaporating MAPbI_3 sandwiched between both organic charge transport layers on top of rigid and flexible substrates.^[12,13] Yang et al. developed an alternating vacuum deposition method, by alternating PbCl_2 and $\text{CH}_3\text{NH}_3\text{I}$ precursor layers, reaching a PCE of 16.03%.^[14] Then, in 2016, Momblona et al. presented a direct comparison between fully sublimed n–i–p and p–i–n devices containing the same materials

N. Klipfel, Dr. C. Momblona, Dr. H. Kanda, Dr. M. D. Mensi, C. Liu, Dr. C. Roldán-Carmona, Prof. M. K. Nazeeruddin
Group for Molecular Engineering of Functional Materials
Institute of Chemical Sciences and Engineering
École Polytechnique Fédérale de Lausanne (EPFL Valais Wallis)
Rue de l'Industrie 17, CH-1951 Sion, Switzerland
E-mail: cristina.rolandancarmona@epfl.ch; mdkhaja.nazeeruddin@epfl.ch

Dr. N. Shibayama
Faculty of Biomedical Engineering
Graduate School of Engineering
Toin University of Yokohama
1614 Kurogane-cho, Aoba, Yokohama, Kanagawa 225-8503, Japan

Dr. Y. Nakamura
Japan Synchrotron Radiation Research Institute (JASIR)
Spring-8, 1-1-1, Kouto, Sayo-cho, Sayo-gun 679-5198, Hyogo, Japan

 The ORCID identification number(s) for the author(s) of this article can be found under <https://doi.org/10.1002/solr.202100191>.

© 2021 The Authors. Solar RRL published by Wiley-VCH GmbH. This is an open access article under the terms of the Creative Commons Attribution License, which permits use, distribution and reproduction in any medium, provided the original work is properly cited.

DOI: 10.1002/solr.202100191

and layers but with inverted deposition order leading to efficiencies exceeding 16.5% for p-i-n and 20% for n-i-p devices.^[15] Also, in 2019, the group of Lohmann et al. published a first study targeting the crystal growth modes in the coevaporation of MAPbI₃.^[16] In 2017, Borchert et al. used the scalable coevaporation method to fabricate formamidinium-based perovskite devices reaching efficiencies of 14.2% (8 cm²).^[17] Olthof and Meerholz described for the first time the substrate influence on coevaporated perovskite^[18] and Zhu et al. demonstrated coevaporated CsMAPbI₃ devices reaching efficiencies as high as 20.13%.^[19] Hutter et al. reported in the same year the sequential vapor deposition of all-inorganic CsPbI₃, reaching a PCE of 8%.^[20] Multication and multihalide perovskite has been demonstrated to be deposited by vacuum-based techniques. For example, large-bandgap perovskite devices of MAPb(Br_{0.2}I_{0.8})₃ were for the first time demonstrated in 2018 by the group of Bolink et al., reaching 15.9%, which was followed then by the demonstration of narrow-bandgap FAPb_{0.5}Sn_{0.5}I₃ reaching a PCE of 13.98% in 2019.^[21,22] In 2020, the publications using coevaporation as the main fabrication technique were significantly rising. In 2020 Momblona et al. demonstrated that coevaporation is also an interesting method for the fabrication of lead-free perovskites, such as methylammonium bismuth iodide.^[23] In the same year also Chiang et al. demonstrated the multisource evaporation of p-i-n FA_{0.7}Cs_{0.3}Pb_{(10.9}Br_{0.1})₃ reaching 18.2% efficiency.^[24] Wang and co-workers demonstrated the fabrication of mini-modules reaching efficiencies of 20.28% (21 cm²).^[25]

Unfortunately, reproducing this level of performance exceeding 20% remains elusive. Indeed, a deeper understanding of the evaporation process and resulting perovskites, in comparison to those reported from solution, is still limited. For example, it is not clear if thermally coevaporated methylammonium lead iodide (MAPbI₃) can crystallize in the cubic phase with alternating PbI₂ amount, therefore altering the thermodynamic equilibrium established for the crystal phase.^[26] Ávila et al. also reported unusual values of the refractive index, suggesting optical properties distinct from those prepared from solution.^[27] In addition, contrary to previous studies of solution-based

processes, Lohmann et al., Kim et al., and Jiang et al. observed that smaller crystals prepared via sublimation have a positive impact on device efficiency.^[16,28,29] In addition, little attention has been given to the surface of deposition and the possible interactions occurring via sublimation.^[18,30,31] Therefore, despite the apparent simplicity and increasing effort to understand the deposition process, thermal coevaporation of hybrid perovskites remains unclear, and only a limited number of research teams report satisfactory results.^[15,16,19,25,32]

Here, we present a systematic study investigating fundamental aspects of the thermal coevaporation of MAPbI₃, the benchmark system with the simplest hybrid composition. Although many variables do influence the vacuum deposition (film thickness, chamber pressure, substrate temperature, or precursor ratio), they are very well established within the field and taken into consideration in every deposition process.

However, here we investigate the crystallization speed and surface chemistry, and their effect on the perovskite work function, morphology, and crystal orientation. Our results demonstrate that these two variables, often neglected, are critical to obtaining reproducible results as they determine the crystal formation, crystal orientation, and film morphology, having an outsized impact on the structural and optoelectronic features. This enables the fine-tuning of crystal formation toward vertically monolithic crystals, providing for the first time high control on crystal growth and orientation on a large-area-compatible technique, which is an imperative requirement to move forward toward commercialization.

2. Results and Discussion

2.1. Material Characteristics

Figure 1 provides a schematic overview of the dual evaporation process and the different charge transport materials used in this study (HTM for holes and ETM for electrons). In brief, MAPbI₃ films were prepared by coevaporating the two starting precursors, CH₃NH₃I and PbI₂, in a 1:1 molar ratio, forming the typical

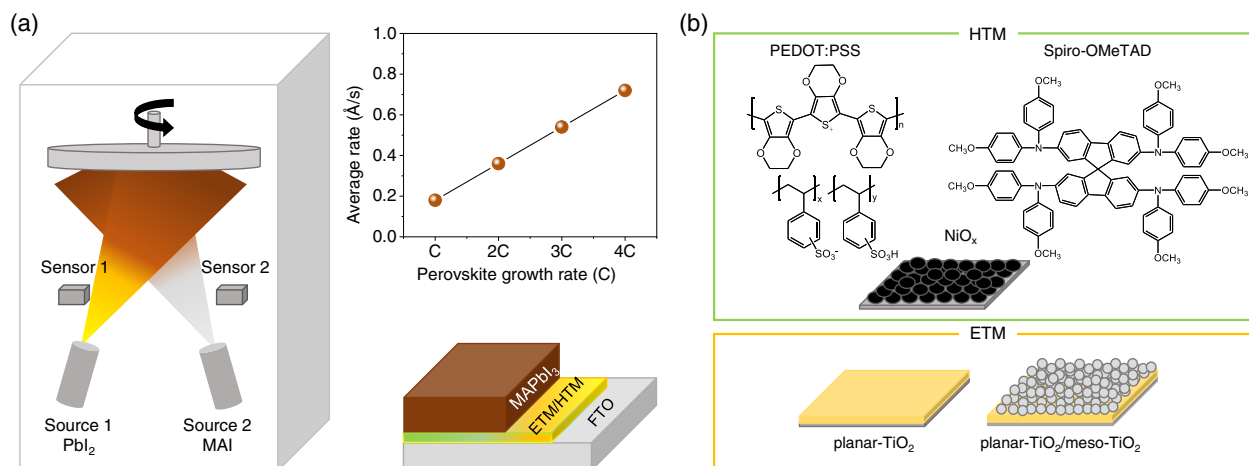


Figure 1. Dual-source evaporation process and device configuration. a) Coevaporation of MAPbI₃ from PbI₂ and MAI precursors at several deposition rates (from C to 4C) and substrate architecture. b) P- and n-type semiconductors (HTM and ETM, respectively) used as underlying charge transport materials.

3D perovskite with tetragonal phase (Figure S1, Supporting Information).^[17] We investigated the effect of the evaporation rate and, therefore, the speed of crystal growth on the perovskite formation. The evaporation rate for PbI_2 was monitored by a quartz crystal microbalance situated above the PbI_2 source. A perovskite growth rate of 0.18 \AA s^{-1} (see specifications in device fabrication) was initially fixed as reference (C) and increased by a factor of 2 ($2C = 0.36 \text{ \AA s}^{-1}$), 3 ($3C = 0.54 \text{ \AA s}^{-1}$), and 4 ($4C = 0.72 \text{ \AA s}^{-1}$) (Figure 1a).

MAPbI₃ films were deposited under different deposition rates while maintaining the same precursor ratio in all cases (Figure S2, Supporting Information). State-of-the-art semiconductors were used as charge transport materials. 2,2',7,7'-Tetrakis[N,N-di(4-methoxyphenyl)amino]-9,9'-spirobifluorene (spiro-OMeTAD), poly(3,4-ethylene dioxythiophene)-poly(styrene sulfonate) (PEDOT:PSS), and NiO_x were chosen as HTMs, and TiO₂ (planar or mesoporous) was used as ETM (Figure 1b).

To initiate the study, we used fluorine-doped tin oxide (FTO) substrates covered with NiO_x as the HTM and deposited MAPbI₃ films ($\approx 1 \mu\text{m}$ thick) at increasing crystal growth rates, ranging from C to 4C. We analyzed the film morphology, surface coverage, and roughness using scanning electron microscopy (SEM) and atomic force microscopy (AFM). The SEM images, shown in Figure S3, Supporting Information, show a polycrystalline morphology, with the estimated grain size distribution varying slightly according to the perovskite growth rate (Figure S4, Supporting Information). Films deposited at a low rate (C) show homogeneous SEM features along the entire film, with an average value of $\approx 237 \text{ nm}$. Similar grain distribution has typically been reported for vacuum-coevaporated perovskites.^[15] Yet, using faster deposition rates (4C) increases the mean value to $\approx 340 \text{ nm}$ and induces the formation of prominent grains over $1 \mu\text{m}$ in diameter (see top-surface SEM; Figure S3a, Supporting Information). A similar trend is observed for the film roughness, as the root-mean-square (RMS) value increases from ≈ 58 to 78 nm under faster growing rates (C–4C) (Figure S5, Supporting Information). This suggests that the roughness of vacuum-deposited perovskites is not necessarily similar to the underlayer, as would generally be expected from a conformal deposition of the film (see also Figure S12, Supporting), but it rather depends on the growing condition selected for the process.

We further investigated the electronic structure using ultraviolet photoelectron spectroscopy (UPS) (Figure S6, Supporting Information). This technique is a powerful tool to access the electronic profile providing relevant information such as the work function (ϕ) and the injection barrier between specific materials. The results, summarized in the energetic profile displayed in Figure 2a, reveal pronounced changes in the perovskite's electronic levels motivated by the different sublimation speeds. As we increase the perovskite growth rate, a small shift in the Fermi level occurs of up to 0.07 eV for 3C and a prominent change in the valence band values (E_{VB}) from -5.37 eV (C) to -5.54 eV (3C) (Figure S6, Supporting Information). Given that MAPbI₃ has a bandgap value of 1.6 eV , this implies that the perovskite gradually changes from p-type to an intrinsic semiconductor character as the growth rate increases from C to 3C. A faster growth rate (4C) induces a reverse valence band shift of 0.11 eV , toward higher binding energy, making the material gain more p-type characteristics. Note that such differences,

emerging exclusively from the various deposition speeds, are paramount for achieving optically aligned electronic levels and therefore efficient charge extraction within the device. We also characterized the materials by UV–vis absorption and photoluminescence (PL) spectroscopy. Contrary to UPS, these techniques are less sensitive to surface effects and instead provide rich information about the bulk material, facilitating a more complete picture of the layer. The results, shown in Figure 2b,c, reveal significant changes in the shape of the spectra, and a tiny shift in the absorption onset consistent with the UPS trend (see full spectra in Figure S7, Supporting Information). In particular, we highlight the strong redshift occurring in the PL emission for faster depositions, from 1.65 eV (C) to 1.59 eV (3C), which again reverses for very fast crystallizations (4C). We note here that similar effects have been previously ascribed to small changes altering the lattice strain and orbital hybridization of the inorganic skeleton.^[15,24,33–37] In our case, the photophysical scenario is affected by the crystallization dynamics during crystal formation, which may alter factors such as charge dissociation, charge transport, and diffusion length, and consequently the device performance.^[38]

To shed light on the origin of such variations, we further explored the crystallinity of the perovskites by X-ray diffraction (XRD) measurements. Figure S8, Supporting Information, contains the diffraction patterns of NiO_x/MAPbI₃ films grown at increasing crystallization speeds. All films exhibit intense diffraction signals typical of the crystalline tetragonal MAPbI₃ phase (theoretical pattern is included for reference), but there are strong differences in the relative intensity between peaks for the different growing conditions; e.g., the (200) crystal plane disappears with increasing perovskite growth rate in 2C, 3C, and 4C. This phenomenon denotes a nonuniform distribution of the crystallites in the angular space, suggesting plausible film growth along preferred crystal orientations. We verified the out-of plane reflections by using wide-angle X-ray scattering (WAXS), which allows the investigation of crystal planes not accessible by conventional powder XRD.^[39] In the WAXS 2D images, displayed in Figure 2d, the azimuthal intensity distribution correlates to the orientation of the planes; therefore, uniform intensity along the Debye–Scherrer ring (e.g., 4C at $q_z = 1.0, 2.0 \text{ \AA}^{-1}$) indicates no preferred crystal orientation. By contrast, the high-intensity red spots at $q_z = 1.0, 2.0 \text{ \AA}^{-1}$ for C, 2C, and 3C suggest specific out-of-plane orientations. To better visualize these changes, we selected the Debye–Scherrer ring corresponding to the (220) lattice plane at $q_z = 2.0 \text{ \AA}^{-1}$ (Figure 2e) and integrated the intensity along the azimuthal angle between $q_z = 2.00$ and 2.03 \AA^{-1} (see Supplementary Notes). The intensity profile, shown in Figure 2e, consists of an intense peak for C, 2C, and 3C, suggesting a large portion of crystals oriented along χ values of 75° – 78° (see specific values in the inset). Contrary to what is expected from crystal growth theory,^[40] faster perovskite growth rates (3C) decrease peak broadness and induce more prominent orientations up to 4C, the latest with broader distribution of crystals aligning between 70° and 90° (see schematic number of brown (oriented) versus white (non-oriented) cubes in the inset). Interestingly, the changes in orientation follow a similar trend to that observed for the UPS, suggesting strong correlations between the optical properties and the crystallization kinetics.

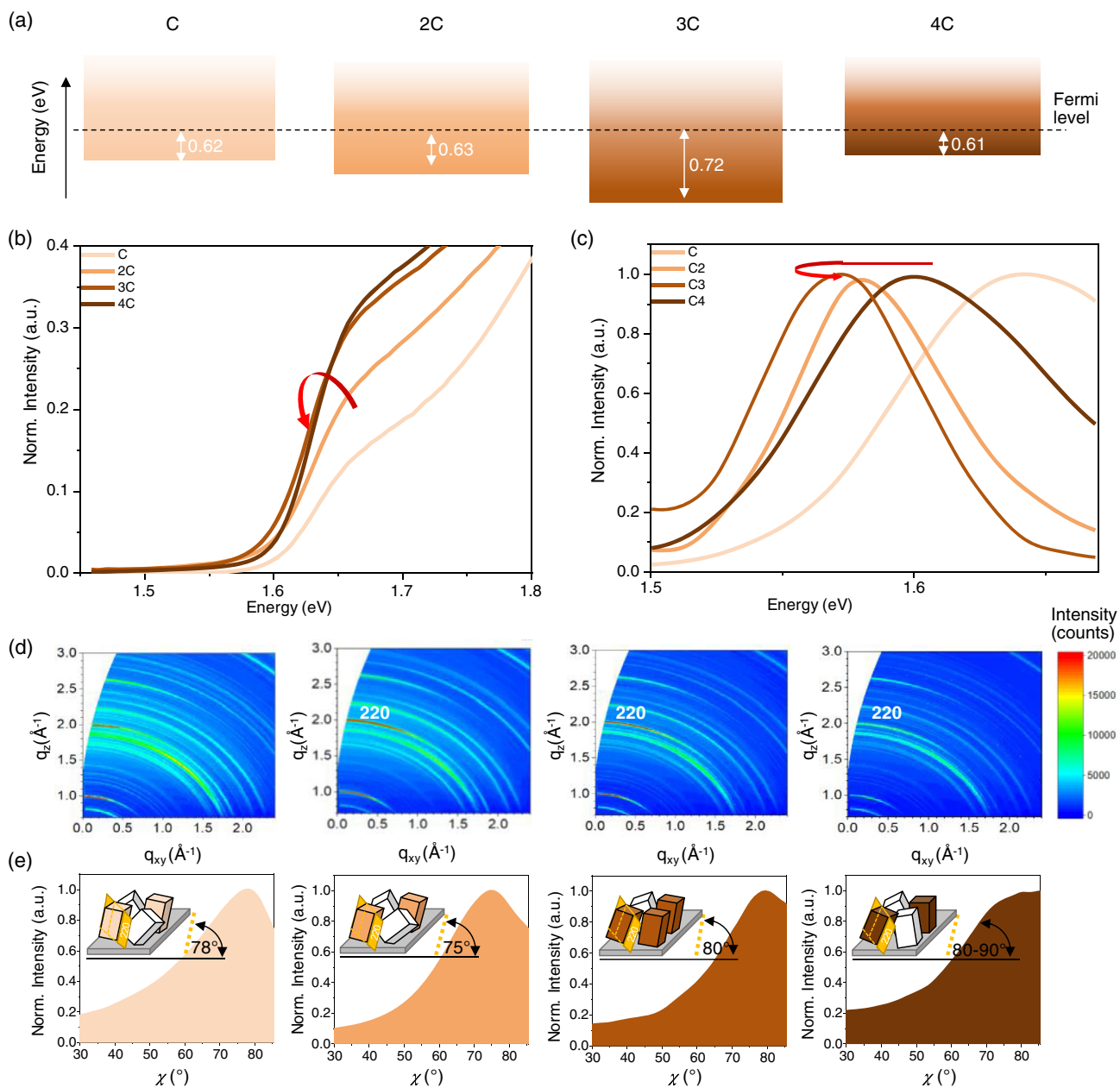


Figure 2. MAPbI₃ films grown on NiO_x. a) Energy levels extracted from UPS measurements of films grown at several deposition rates (from C to 4C). b) UV-vis absorption and c) PL spectra of films shown in (a) (excitation wavelength $\lambda = 450$ nm). d) WAXS images of films shown in (a). e) Integration of the azimuthal intensity along the 220 reflex in WAXS. Inset: schematic of 220 lattice plane orientation showing out-of-plane orientation relative to the substrate (cubes in different brown shading: 220 lattice plane tilted 78° (C), 75° (2C), and 80° (3C) from the substrate). Note the apparent trend in 4C of intensity between 80° and 90°. Fewer white cubes indicate more preferred orientation.

We performed similar experiments on perovskite films deposited on TiO₂, to compare with a metal oxide semiconductor having a very different work function value. Figure S9 and S10, Supporting Information, show similar changes to those observed in NiO_x for the optoelectronic properties after varying the perovskite growth rate, providing strong variations in the Fermi level, bandgap, and PL peak position. It can also be noted that varying the deposition rate on both metal oxides, NiO_x and

TiO₂, promotes a similar change in the orientation of the 220 lattice plane, and could be potentially used to induce specific crystal orientations. Such effects, promoted by the deposition speed, have not been previously observed and point out the perovskite growth rate as a key parameter affecting vacuum-deposited perovskites. We note that given that vacuum deposition allows an easy control of this parameter, it could be plausibly used to minimize the morphological and energetic disorder of

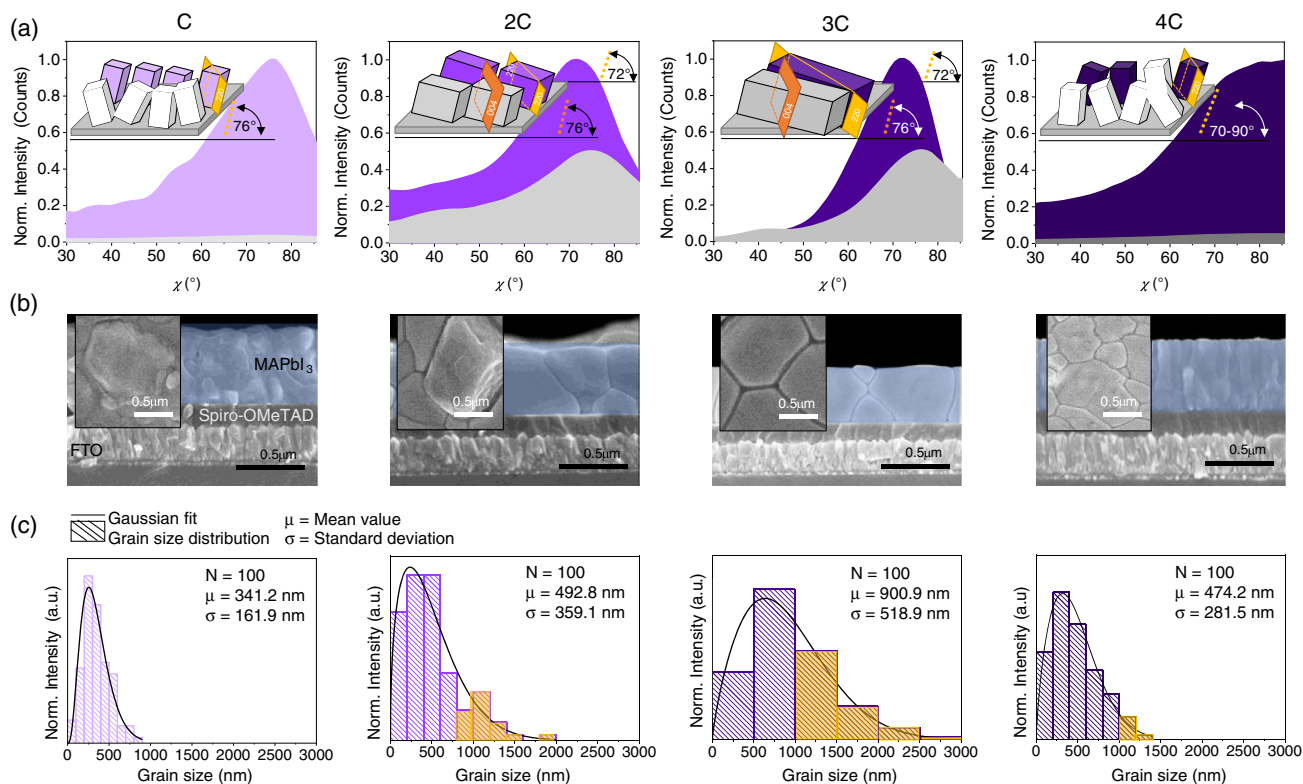


Figure 3. MAPbI₃ films grown on spiro-OMeTAD. a) Integration of the azimuthal intensity along the 220 reflex (2.0 \AA^{-1}) in WAXS for films crystallized at different deposition rates (from C to 4C). Inset: schematic of grains with the 220 lattice plane showing out-of-plane orientation (indicated by cubes with purple shading: tilted 76° (C), 72° (2C), and 72° (3C) from the substrate). Grains with the 004 lattice plane showing in-plane orientation (indicated by cubes with gray shading: tilted 72° (C), 76° (2C), and 76° (3C) from the substrate). Note the apparent trends for peak intensity angles between 70° and 90° of the 220 lattice plane (4C). Fewer white cubes indicate more preferred orientation. b) Cross-section and top-view (inset) SEM images of MAPbI₃ formed on spiro-OMeTAD substrates. c) Estimated grain-size distribution of the perovskite layers.

the films. Interestingly, spiro-OMeTAD, the archetypal organic HTM used in PSCs, showed a rather different behavior (Figure 3a). We fabricated films using the same conditions as described before (C–4C) and integrated the azimuthal intensity of the Debye–Scherrer ring at $\approx 2.0 \text{ \AA}^{-1}$ of the WAXS data. The crystal orientation was barely affected by the perovskite growth rate (Figure 3a, from C to 4C), and films exhibit pronounced out-of-plane crystal-alignments centered at $\chi = 72^\circ$ (see inset). Similar to the previous results, increasing the growth rate produces a sharper peak for the 220 lattice plane, providing the strongest preferred orientations for perovskites grown at 3C. Interestingly, a second Debye–Scherrer ring at $1.97\text{--}2.00 \text{ \AA}^{-1}$ (corresponding to the (004) lattice plane, Figure S11, Supporting Information) revealed an additional orientation appearing only for 2C and 3C, which is perpendicular to the prior. We note that the tetragonal (220) diffracts at very close 2θ angles than that of (004), and therefore both peaks frequently overlap. This is the situation observed in Figure 2 for films grown on NiO_x. However, if we inspect the $q_z \sim 2.0 \text{ \AA}^{-1}$ region in Figure S11, diffraction lines appear always at either 1.99 or 2.01 \AA^{-1} , or both of them, depending on the growing conditions. These lines are assigned to (220) and (004), respectively, and can be used to identify the planes in the 2D-WAXS images.

Therefore, films made under such conditions exhibit highly oriented crystals with both out-of-plane and in-plane crystal orientations at $\chi_{220} = 72^\circ$ and $\chi_{004} = 76^\circ$. Note, the top and cross-section SEM images (Figure 3b) also show strong variations in film morphology and grain size, according to the speed of crystallization. Although a deeper analysis via electron backscatter diffraction (EBSD) or transmission electron microscopy (TEM) has not been performed, in the following lines we will refer as grains to the features observed in SEM, as commonly used in the literature. Therefore, the grain sizes here are estimations used to describe a general trend that we see in morphology. Starting with smaller grains (C), a striking difference appears for 2C and 3C, providing uniform and large crystals of over $\approx 1 \mu\text{m}$ diameter (see Figure 3c). In particular, we highlight the monolithic growth of the crystal in the out-of-plane direction, especially remarkable for layer 3C, in which the grains align perfectly in the vertical direction (see Figure 3b, rate 3C). Only at the highest speed (4C) do grain sizes become smaller and more randomly oriented, forming a uniform nanorod-like morphology lined up along the substrate (see grain size distribution in Figure 3c). We note that obtaining such a morphology and homogeneous distribution is very challenging in vacuum-codeposited films, and comparable morphologies have been only acquired under very severe temperature treatments (-2°C).¹¹ The AFM

measurements, shown in Figure S12, Supporting Information, also showed different roughness according to the deposition rate (1C, RMS = 63.08 nm; 2C, RMS = 50.05 nm; 3C, RMS = 38.62 nm; 4C, RMS = 46.81 nm), differing substantially from that of the underlayer (RMS = 2.96 nm). These changes reveal for the first time the dual impact of the crystal growth rate and interfacial chemistry on vacuum-deposited perovskites, which calls for deeper analysis to explore their origin and repercussions on thin films.

To specifically target the effects induced by the interface, we investigated the crystallization dynamics on several underlying materials at a fixed deposition rate and thickness (3C = 0.54 Å s⁻¹, 500 nm), and extended the investigation to alternative state-of-the-art semiconductors such as PEDOT:PSS and meso-TiO₂. Due to the versatility of thermal evaporation, several substrates could be targeted in a single evaporation, therefore ensuring that the interface is the unique variable between films. The electronic structure, optical properties, and elemental composition of the resulting films are summarized in Figure 4. Results show that perovskites undergo a pinning in the Fermi level with the valence band onset determined by the substrate, but contrary to previous reports using different semiconductors, the changes barely deviate according to the p- or n-type character, while they mostly do according to the chemical nature of the contacting material (see values for metal oxides in Figure 4a).^[41–43] Specifically, perovskites grown on p-type semiconductors with similar ϕ values but different surface chemistry (Figure 4a) exhibit large changes on the Fermi level and valence band onset, even for 500 nm films. We observed values of $\phi_{\text{Per/NiO}_x} = 4.82$ eV, $\phi_{\text{Per/spiro-OMeTAD}} = 4.67$ eV, $\phi_{\text{Per/PEDOT:PSS}} = 4.88$ eV, showing differences of >0.2 eV between spiro-OMeTAD and PEDOT:PSS (see ϕ values for the bare underlayer in Figure S13, Supporting Information). Similarly, the valence band onsets

shift by 0.72, 0.81, and 0.69 eV to the Fermi level for NiO_x, spiro-OMeTAD, and PEDOT:PSS, respectively.

Such strong variations are in line with previous reports describing plausible chemical interactions at the perovskite/metal-oxide interface.^[18] However, these interactions are expected to exclusively affect the first 30 nm of the seeding layer, leading to identical perovskite composition and crystal growth over 30 nm. In our case, the effects extend to the whole perovskite material (500 nm), thus affecting also the bulk optical and electronic features (Figure 4c and Figure S14, Supporting Information). We further investigated the chemical environment of nitrogen (N 1s), iodine (I 3d_{5/2}), and lead (Pb 4f_{7/2}) signals by X-ray photoelectron spectroscopy (XPS) (Figure S15, Supporting Information). To avoid any surface contamination, we transferred the fresh samples directly from the glove box into the XPS machine via a transfer vessel. We observe the typical photoemission peak attributed to the NH₃⁺ group in methylammonium (402.6 eV), sharp double peaks assigned to I 3d (≈619.5 eV for I 3d_{5/2} and ≈631 eV for I 3d_{3/2}) and Pb⁺² (≈138.6 eV for Pb 4f_{7/2} and ≈143.4 eV for Pb 4f_{5/2}), which confirm the formation of Pb–I bonds. No metallic lead (≈136.5 and ≈141.5 eV) is detected on any layer. Despite this confirmation, the perovskite composition at the surface shows significant changes with respect to the underlayer: Although perovskites form similarly on metal oxides, strong differences appear in those grown on organic p-type layers (Figure 4b, Table 1).

Comparing the three types of HTMs displayed in Figure 4 (organic and inorganic), the relative I:Pb ratio varies by 3.24, 3.13, and 2.86 for NiO_x, PEDOT:PSS, and spiro-OMeTAD, respectively, suggesting an excess of PbI₂ dominating the perovskite on spiro-OMeTAD. As perovskites crystallize in the same evaporation process with a 1:1 fixed precursor ratio, it is the underlayer that determines the final chemical composition and energetic features of the coevaporated perovskite.

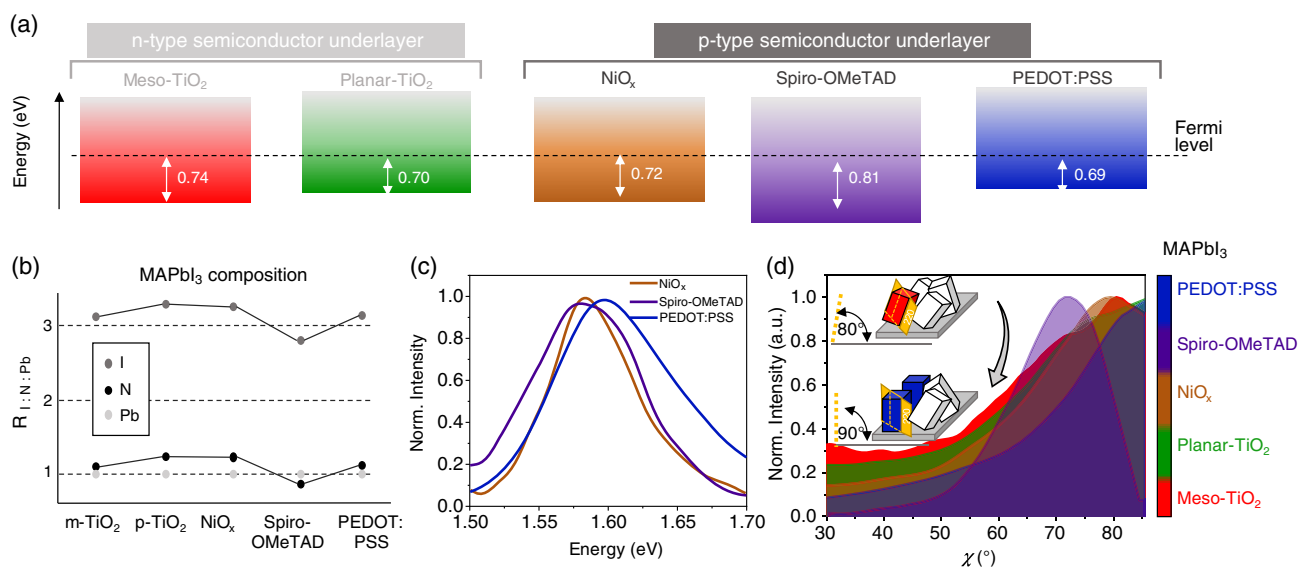


Figure 4. MAPbI₃ films deposited on several semiconductors. a) Energy levels extracted from UPS data of perovskites formed on top of n- and p-type underlayers prepared under the same evaporation condition (3C). b) Compositional data extracted from XPS for the elements lead (Pb 4f), nitrogen (N 1s), and iodide (I 3d). c) PL spectra recorded for all conditions. d) Integration of the azimuthal intensity distribution of the 220 reflex in the WAXS data. Inset: schematic of grains with the 220 lattice plane showing out-of-plane alignment relative to the substrate (for perovskite on meso-TiO₂, red cube 220 lattice plane 80° from substrate; for perovskite on PEDOT:PSS, blue cube 220 lattice plane 90° from substrate).

Table 1. Compositional analysis of MAPbI₃ deposited on p- and n-type semiconductors. Atomic ratios are extracted from the XPS data shown in Figure S15, Supporting Information.

Type of underlayer	Atomic ratio			
	I:Pb		N:Pb	
	Experimental	Theoretical	Experimental	Theoretical
Meso-TiO ₂	3.05	–	0.99	–
Planar TiO ₂	3.29	–	1.19	–
NiO _x	3.24	3	1.19	1
Spiro-OMeTAD	2.86	–	0.87	–
PEDOT:PSS	3.13	–	1.08	–

Such results, which could stem from the various crystallographic changes and surface properties induced by each underlayer, have important implications in device optimization and upscaling of fabrication, as well as device reproducibility from different laboratories.^[44]

Indeed, strong variations in crystal orientation (500 nm) are detected from the azimuthal integration of the 220 lattice plane for each underlayer (Debye–Scherrer ring at 2.0 Å⁻¹) (Figure 4d). While the meso-TiO₂ favors a uniform random crystal distribution, few preferred orientations emerge on planar metal oxides but they do become apparent on the organic semiconductors. As discussed for Figure 3, such preferred crystal orientations observed for spiro-OMeTAD and PEDOT:PSS do not heavily depend on the perovskite growth rate, denoting a key role of the surface chemistry of the underlayer in dictating specific crystal alignments, paramount to controlling the crystallization

via thermal coevaporation (see also Figure S16, Supporting Information). Interestingly, strong interactions at the interfaces with methoxy anchors (present in spiro-OMeTAD) (Figure 1b) and thiophene derivatives (present in PEDOT:PSS) (Figure 1b) have been previously reported for perovskites processed via solution.^[45] We therefore believe that such interfacial interactions could become crucial on vacuum-deposited perovskites, providing an effective tool to fine-tune the crystal growing into specific lattice orientations.

To gain insight into this phenomenon, we investigated the WAXS images for perovskite seeding layers of 35 nm, exclusively targeting the region in direct contact with the interface. **Figure 5a** and **Figure S17a**, Supporting Information, show evidence of ring patterns without preferred crystal orientations for layers grown on metal oxides but a clear out-of-plane orientation for the two organic interfaces. Importantly, a single-crystalline orientation emerges on spiro-OMeTAD, denoting a very consistent crystal growth induced by methoxy groups. We note that having such a strong out-of-plane crystal orientation remains to date of high interest for many optoelectronics, offering the opportunity to more closely approach the Shockley–Queisser limit in photovoltaics, as compared to polycrystalline layers.^[5,6,45–48] This also provides additional support to our previous assessment, demonstrating interfacial-guided orientations induced by the underlying surface.

Our data also suggest that the seeding composition highly depends on the type of underlayer, showing preferential accumulation of PbI₂ precursor on the organic interlayers. Moreover, these seeding layers will determine the upcoming crystal growth and film composition obtained during the deposition process, as also revealed by the *q*-pattern evolution in **Figure 5b**. We note that previous reports based on glass surfaces have proposed an initial

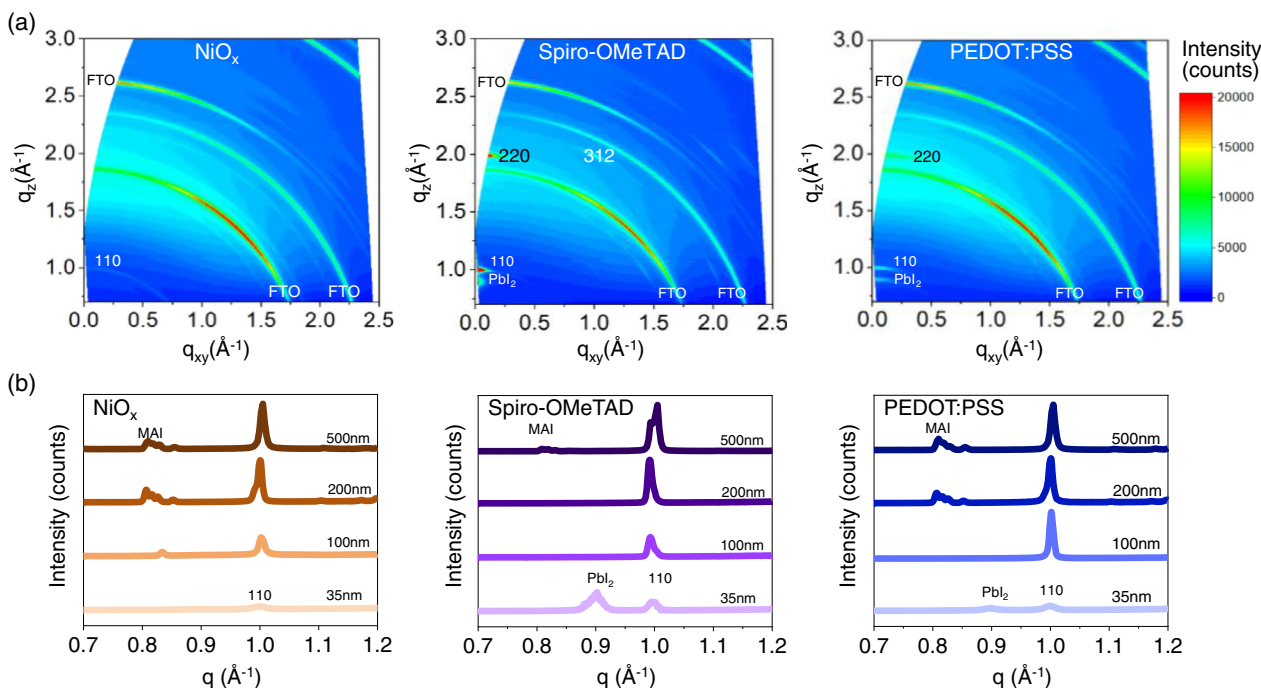


Figure 5. Evolution of vacuum-deposited MAPbI₃ layers. a) WAXS images of 35 nm films grown on NiO_x, spiro-OMeTAD, and PEDOT:PSS. Diffractions related to FTO and PbI₂ are indicated in the label. b) Evolution of XRD patterns with increasing film thickness.

nucleation of MAPbI₃ islands (with 8 nm height) via Volmer–Weber-type growth, which explains the formation of multiple small grain sizes in the film.^[32] However, here we see that small grains are not the unique possible morphology in evaporated films, and instead it is highly influenced by the type of underlayer and rate of evaporation, resulting in films with different properties and grain sizes (Figure S4, Supporting Information, and Figure 3c). We further observe that the initial accumulation of PbI₂ on organic substrates, absent for metal-oxide substrates, rapidly vanishes as the layer evolves from 35 to 500 nm, maintaining a stoichiometric film for organic underlayers ≤200 nm thick. This is concomitant to a gradual accumulation of MAI occurring for perovskites grown on metal oxides ($q = 0.8 \text{ \AA}^{-1}$) (Figure S17a,b, Supporting Information), which is only detected at ≥200 nm in PEDOT:PSS (almost absent for those grown on spiro-OMeTAD, 500 nm). Given that the films crystallized under the same sublimation process, the surface chemistry of the underlayer might determine which precursor adsorbs first, resulting in different seeding centers from where the perovskite evolves. In addition, as the final stoichiometry is substantially influenced by the two parameters here discussed, it is no longer adequate to generalize with a specific precursor ratio to achieve an optimal perovskite, as this must be independently optimized with the specific underlayer and deposition rate.

2.1.1. Device Performance

We verified the impact of the several crystallizations on device performance by selecting spiro-OMeTAD as the template underlayer and fine-tuning the crystal arrangements via the deposition rate. We embodied 500 nm layers into p–i–n devices, using C₆₀/BCP as the ETM and chromium/gold as the metallic electrode (see device configuration in Figure 6a). We note that this simple approach enabled the preparation of perovskite films with micrometer-sized grains of identical orientation, as demonstrated in the 2D-XRD and SEM images displayed in Figure 6. Such results underline the high potential of tuning the deposition rate in controlling the crystal formation toward perfect crystal orientation.

Figure 6d,e and Figure S18, Supporting Information, summarize the main photovoltaic parameters obtained for each type of layer, confirming a direct relation between crystallization and device performance, providing the best results for the highest oriented films. Indeed, the short current density (J_{sc}) gradually increases when changing the perovskite growth rate from C to 3C ($J_C = 18.45 \text{ mA cm}^{-2}$; $J_{2C} = 18.90 \text{ mA cm}^{-2}$; $J_{3C} = 19.94 \text{ mA cm}^{-2}$) but strongly reduces for 4C ($J_{4C} = 17.66 \text{ mA cm}^{-2}$) (Table S1, Supporting Information), in agreement with the external quantum efficiency (EQE) spectra (Figure 6e). A similar trend is observed for the fill factor (FF),

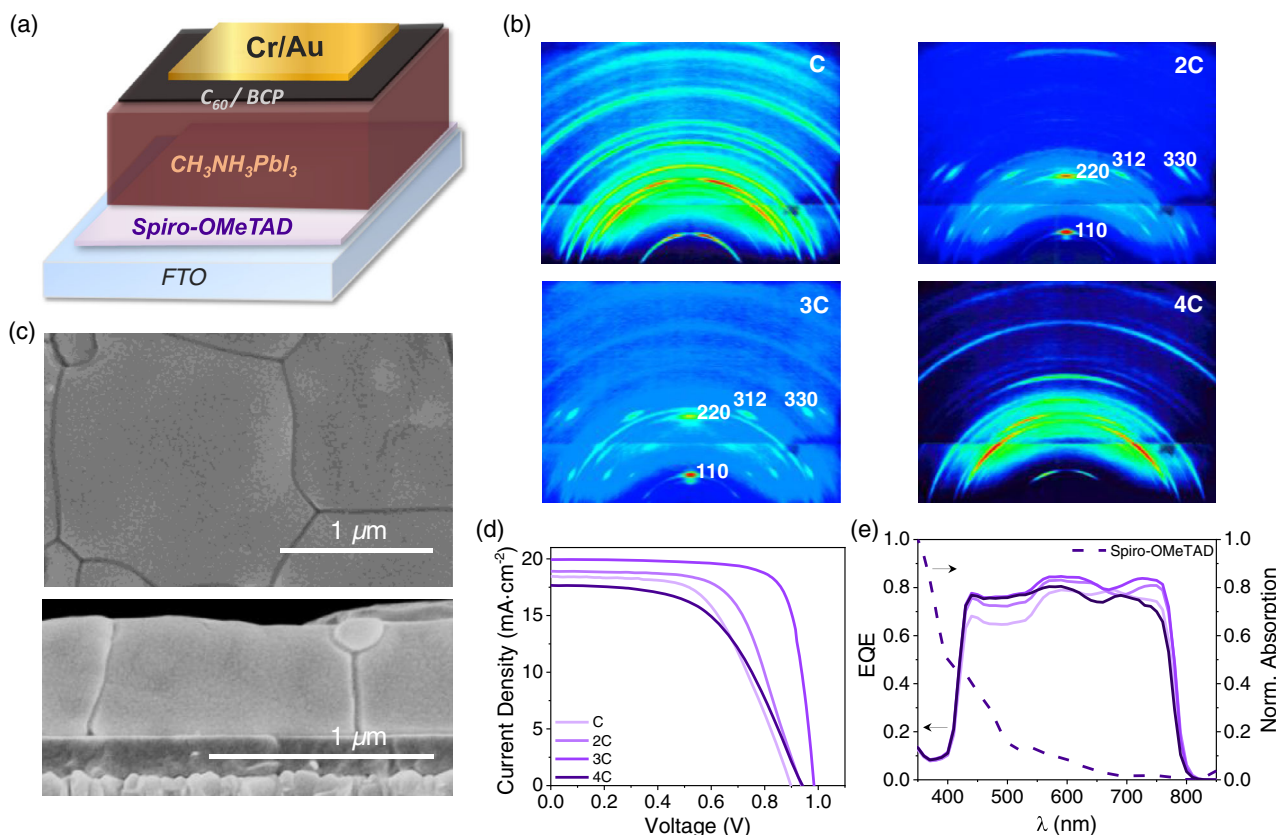


Figure 6. Influence of the deposition rate on crystallization and device performance. a) Scheme of p–i–n architecture used for the PSCs. b) 2D-detector images of 500 nm MAPbI₃ grown on spiro-OMeTAD at different deposition rates (from C to 4C). The spots indicate the preferred out-of-plane orientation. c) Top- and cross-section SEM of MAPbI₃ films (3C). Scale bar: 1 μm. d) *J*–*V* curves and e) EQE spectra of typical devices including absorption spectra for underlayer spiro-OMeTad containing films shown in (a) and (b).

which improves by 33% when shifting from C to 3C, boosting the PCE from 9.46% to 15.19%. Notably, despite the high photon-to-current conversion efficiency of $\approx 80\%$ being observed in the visible range (resulting in an integrated current of 17.74, 19.02, 19.52, and 18.21 mA·cm⁻² for C to 4C, respectively), no signal is detected in the region below 400 nm. We explain this by considering the high absorption of spiro-OMeTAD in the blue spectral region below 450 nm, which limits the photogeneration of carriers in the high-energy zone. We note that this absorption further extends up to 700 nm (see Figure 6e) behaving as an optical filter for the incoming light. This partially explains the moderate PCE values observed for this specific p–i–n configuration and invites the designing of more transparent alternatives containing methoxy-enriched interfaces, such as spiro-OMeTAD. Cell growth at 2C and 3C crystallization speeds also showed improved stability when measured at maximum power point (MPP) tracking and continuous light illumination, as shown in Figure S19, Supporting Information.

3. Conclusion

A proper combination of the surface chemistry of the underlayer and speed of sublimation in vacuum-deposited perovskites allows, for the first time, full control over the morphology, chemical composition, and crystal alignment. To date, this has been difficult to achieve. These variables, usually neglected in the literature, may be a major source of irreproducibility when not carefully chosen, and must therefore be explicitly indicated in all future publications. However, when properly combined these parameters provide an opening for fine-tuning perovskite films toward specific crystal quality and orientation. This enables the fabrication of monolithic micrometer-sized crystals with perfect crystal alignment via thermal coevaporation, pushing forward the understanding of irreproducibility sources in a large-area-compatible technique, which is a prerequisite for any future attempt at commercialization.

4. Experimental Section

Thin-Film and Device Fabrication: Thin films were fabricated on FTO-coated glass substrates (TEC-15AX, NSG group) previously cleaned by a sequential sonication treatment in a 2% Hellmanex solution, acetone, and isopropanol, followed by UV–ozone treatment for 15 min. A compact blocking layer of TiO₂ (planar TiO₂, 30 nm thick film) was then deposited on the FTO-coated glass substrate by spray pyrolysis, using a titanium diisopropoxide bis(acetylacetonate) (TAA) solution (Sigma-Aldrich) in ethanol (1 mL of TAA in 15 mL ethanol) and then sintered at 450 °C for 30 min. A 200 nm thick layer of mesoporous TiO₂ (meso-TiO₂, 30 NR-D titania paste, Dyesol) was prepared from an ethanol dispersion (1 g titanium oxide nanoparticle paste in 9 mL ethanol) and spin coated at 2000 rpm, for 15 s (acc. 1000). Afterward, the samples were sintered at 500 °C for 30 min in air. The NiO_x layers were prepared by the spray pyrolysis deposition method using a nickel acetate acetylacetonate (Sigma-Aldrich) solution in acetonitrile (0.04 M). The deposition temperature was 500 °C and was kept for 20 min. The spiro-OMeTAD (Merck) underlayers were spin coated at 4000 rpm for 30 s (acc. 1000 rpm s⁻¹) from a chlorobenzene solution (80 mg in 1023 μL, 60 mM). The solution contained the dopants: bis(trifluoromethane)sulfonimide lithium salt (Li-TFSI) (19 μL from a 517 mg mL⁻¹ stock solution in acetonitrile), *tert*-butylpyridine (TBP) (32 μL) and tris(2-(1 *H*-pyrazol-1-yl)-4-*tert*-butylpyridine)cobalt(II) di[bis(trifluoromethane)sulfonimide] (FK209 Co(II)TFSI

salt) (14 μL from a 517 mg·mL⁻¹ stock solution in acetonitrile). PEDOT:PSS (CLEVIOS PVP Al 4083, Heraeus) underlayers were prepared via spin-coating. The solution was placed in an ultrasonic bath for 15 min to reduce possible agglomeration of the material. Prior to the deposition, the cleaned FTO substrates were treated with UV/O₃ for 30 min to improve the wetting of the solution on the substrate. The PEDOT:PSS dispersion was filtered with a PTFE 0.22 μm pore size filter and spin coated at 1000 rpm for 50 s (acc. 500 rpm s⁻¹). The layers were annealed at 150 °C for 15 min in air.

The prepared layers were transferred to the PRO Line PVD 75 vacuum chamber from Kurt J. Lesker Company equipped with four thermally controlled sources. The crucibles were filled with the perovskite precursors, PbI₂ and MAI, and heated until the sublimation temperatures of 277 and 136 °C for C, 297 and 139 °C for C2, 298 and 131 °C for C3, and 319 and 165 °C for C4 at a vacuum pressure of $\approx 1 \times 10^{-6}$ mbar. During perovskite deposition, the deposition rate of each precursor was kept constant and monitored by independent quartz microbalance crystal sensors (QCMs). The substrates were kept at room temperature and under rotation of 5 rpm.

For device fabrication, the FTO-coated substrates were chemically etched with Zn powder and HCl solution. Once the perovskite layer was deposited, 20 nm of C₆₀ (Sigma-Aldrich, 99.9%) was thermally evaporated followed by 3 nm of BCP (Sigma-Aldrich, 99.9%). Finally, 1 nm Cr and 70 nm Au were deposited by thermal evaporation as top electrode.

Thin-Film Characterization: The XRD patterns of the prepared films were measured using a D8 Advance diffractometer from Bruker (Bragg-Brentano geometry, with an X-ray tube Cu K α , $\lambda = 1.5406$ Å). The absorption spectra were registered with a Lambda 950S spectrophotometer (PerkinElmer, Inc.). Steady-state photoluminescence (PL) measurements were recorded with an LS-55 fluorescence spectrometer (PerkinElmer, Inc.), at an excitation wavelength $\lambda = 450$ nm. 2D-detector images were measured on a Bruker D8 Venture equipped with a Photon 100 detector using a microfocused Molybdenum Imus 2.0 source. Images were exposed at 120 s. The films were mounted on a standard Huber goniometer head by means of a custom-made magnetic adapter pin. Films were positioned vertically during measurement to choose the incidence angle, which was between $2\theta = 10^\circ$ and $\Omega = 3^\circ$. 2D images were visualized and processed using Apex3 and EVA. WAXS patterns represented in reciprocal lattice space were measured at the SPring-8 on beamline BL19B2. The sample was irradiated with an X-ray energy of 12.39 keV ($\lambda = 1$ Å) with a fixed incident angle of the order of 6.0° through a Huber diffractometer. The WAXS patterns were recorded with a 2D image detector (Pilatus 300 K).

To evaluate the crystal orientation, we calculated the diffraction intensities along χ -arc $I_q(\chi)$ according to the following equation

$$I_q(\chi) = \int_{q_1}^{q_2} I(q, \chi) dq \quad (1)$$

where q is the magnitude of the scattering vector and χ is the azimuthal angle. To analyze each diffraction peak, the integration interval from q_1 to q_2 was set appropriately.

An ultraviolet photoelectron spectrometer equipped with a He–I source ($h\nu = 21.22$ eV) (AXIS Nova, Kratos Analytical Ltd, UK) was used to measure the valence band energy, Fermi level, and the work function. The Fermi level of the samples was referenced to that of Au, which was in electrical contact with a sample in UPS measurements. The XPS measurements were conducted on a VersaProbe II (Physical Electronics, Inc.) with a monochromatic Al K α X-ray source operating at 1486.6 eV. The spectra were referenced using the Pb 4f signal. Data were processed using CasaXPS.

Device Characterization: J – V curves were measured using a 2400 Keithley system with a Xe lamp Oriol sol3A sun simulator (Newport Corporation), which was calibrated to AM 1.5 G standard conditions using an Oriol 91 150 V reference cell (J – V curves scan rate of 50 mV s⁻¹ and 10 mV voltage step). The light intensity was calibrated with an NREL-certified KG5-filtered Si-reference diode. Shadow masks with a metal

aperture of 0.16 cm² were used to define the active area of the solar. The cells were measured in air, at room temperature, and without encapsulation, at a constant rate 10 mV s⁻¹ for reversed bias after 5 s under light soaking. No antireflective coating was used during the measurement. The stability test was performed as maximum power tracking under 100 mW cm⁻² illumination with an LED power source. The samples were encapsulated in a measurement box that was purged with argon gas at 0% humidity and constantly kept at 25 °C by a cooling system. The EQE was measured with the IQE200B (Oriel) without bias light.

Supporting Information

Supporting Information is available from the Wiley Online Library or from the author.

Acknowledgements

The authors acknowledge funding from the European Union's Horizon 2020 MSCA Innovative Training Network under grant agreement No 764787 and 754462 and the Swiss National Science Foundation (SNSF 20021E_186390). The research leading to these results received funding from the European Union's Horizon 2020 research and innovation program under grant agreement No. 763977 of the PerTPV project. The authors thank P. Schouwink and Y. Nakamura at Univ. Tokyo for joining as co-authors. The WAXS measurements were performed at SPring-8 at BL19B2 with the approval of the JASRI, proposal no. 2018B1809, 2018B1855, and 2018B1862, and the X-ray photoelectron spectroscopy measurement at SPring-8 at BL46XU with the approval of the JASRI, proposal no. 2018B1868 and NS thanks to the Foundation for Promotion of Material Science and Technology of Japan (MST) research grant. The authors thank Martin Adams for assistance during final manuscript preparation.

Conflict of Interest

The authors declare no conflict of interest.

Data Availability Statement

Research data are not shared.

Keywords

electronic structures, highly oriented perovskites, vapor deposited photovoltaics

Received: March 17, 2021
Revised: May 29, 2021
Published online: June 26, 2021

- [1] C. C. Stoumpos, C. D. Malliakas, M. G. Kanatzidis, *Inorg. Chem.* **2013**, *52*, 9019.
- [2] M. J. P. Alcocer, T. Leijtens, L. M. Herz, A. Petrozza, H. J. Snaith, *Science* **2013**, *342*, 341.
- [3] V. Gonzalez-pedro, E. J. Juarez-perez, W. Arsyad, E. M. Barea, F. Fabregat-santiago, I. Mora-sero, J. Bisquert, *Nano Lett.* **2014**, *14*, 888.
- [4] W. J. Yin, T. Shi, Y. Yan, *Adv. Mater.* **2014**, *26*, 4653.
- [5] D. Shi, V. Adinolfi, R. Comin, M. Yuan, E. Alarousu, A. Buin, Y. Chen, S. Hoogland, A. Rothenberger, K. Katsiev, Y. Losovyj, X. Zhang,

- P. A. Dowben, O. F. Mohammed, E. H. Sargent, O. M. Bakr, *Science* **2015**.
- [6] Q. Dong, Y. Fang, Y. Shao, P. Mulligan, J. Qiu, L. Cao, J. Huang, *Science* **2015**, *347*, 967.
- [7] C. Ran, J. Xu, W. Gao, C. Huang, S. Dou, *Chem. Soc. Rev.* **2018**, *47*, 4581.
- [8] T. S. Sherkar, C. Momblona, L. Gil-Escrig, J. Ávila, M. Sessolo, H. J. Bolink, L. J. A. Koster, *ACS Energy Lett.* **2017**, *2*, 1214.
- [9] H. Jin, E. Debroye, M. Keshavarz, I. G. Scheblykin, M. B. J. Roeffaers, J. Hofkens, J. A. Steele, *Mater. Horiz.* **2020**, *7*, 397.
- [10] U.S. Department of Energy, National Renewable Energy Laboratory (NREL). Best Research-Cell Efficiency Chart. http://www.nrel.gov/ncpv/images/efficiency_chart.jpg, (accessed: January 2015)
- [11] M. Liu, M. B. Johnston, H. J. Snaith, *Nature* **2013**, *501*, 395.
- [12] C. Roldán-Carmona, O. Malinkiewicz, A. Soriano, G. Mínguez Espallargas, A. Garcia, P. Reinecke, T. Kroyer, M. I. Dar, M. K. Nazeeruddin, H. J. Bolink, *Energy Environ. Sci.* **2014**, *7*, 994.
- [13] O. Malinkiewicz, A. Yella, Y. H. Lee, G. M. Espallargas, M. Graetzel, M. K. Nazeeruddin, H. J. Bolink, *Nat. Photonics* **2014**, *8*, 128.
- [14] D. Yang, Z. Yang, W. Qin, Y. Zhang, S. Liu, C. Li, *J. Mater. Chem. A* **2015**, *3*, 9401.
- [15] C. Momblona, L. Gil-Escrig, E. Bandiello, E. M. Hutter, M. Sessolo, K. Lederer, J. Blochwitz-Nimoth, H. J. Bolink, *Energy Environ. Sci.* **2016**, *9*, 3456.
- [16] K. B. Lohmann, J. B. Patel, M. U. Rothmann, C. Q. Xia, R. D. J. Oliver, L. M. Herz, H. J. Snaith, M. B. Johnston, *ACS Energy Lett.* **2020**, *5*, 710.
- [17] J. Borchert, R. L. Milot, J. B. Patel, C. L. Davies, A. D. Wright, L. Martínez Maestro, H. J. Snaith, L. M. Herz, M. B. Johnston, *ACS Energy Lett.* **2017**, *2*, 2799.
- [18] S. Olthof, K. Meerholz, *Sci. Rep.* **2017**, *7*, 1.
- [19] X. Zhu, D. Yang, R. Yang, B. Yang, Z. Yang, X. Ren, J. Zhang, J. Niu, J. Feng, S. Liu, *Nanoscale* **2017**, *9*, 12316.
- [20] E. M. Hutter, R. J. Sutton, S. Chandrashekar, M. Abdi-Jalebi, S. D. Stranks, H. J. Snaith, T. J. Savenije, *ACS Energy Lett.* **2017**, *2*, 1901.
- [21] N. Droseros, G. Longo, J. C. Brauer, M. Sessolo, H. J. Bolink, N. Banerji, *ACS Energy Lett.* **2018**, *3*, 1458.
- [22] A. M. Igual-Muñoz, J. Ávila, P. P. Boix, H. J. Bolink, *Sol. RRL* **2020**, *4*, 1.
- [23] C. Momblona, H. Kanda, A. A. Sutanto, M. Mensi, C. Roldán-Carmona, M. K. Nazeeruddin, *Sci. Rep.* **2020**, *10*, 1.
- [24] Y. H. Chiang, M. Anaya, S. D. Stranks, *ACS Energy Lett.* **2020**, *5*, 2498.
- [25] J. Li, H. Wang, X. Y. Chin, H. A. Dewi, K. Vergeer, T. W. Goh, J. W. M. Lim, J. H. Lew, K. P. Loh, C. Soci, T. C. Sum, H. J. Bolink, N. Mathews, S. Mhaisalkar, A. Bruno, *Joule* **2020**, *4*, 1035.
- [26] F. Palazon, D. Pérez-del-Rey, B. Dänekamp, C. Dreessen, M. Sessolo, P. P. Boix, H. J. Bolink, *Adv. Mater.* **2019**, *31*, 1.
- [27] J. Ávila, C. Momblona, P. Boix, M. Sessolo, M. Anaya, G. Lozano, K. Vandewal, H. Mínguez, H. J. Bolink, *Energy Environ. Sci.* **2018**, *11*, 3292.
- [28] B. S. Kim, G. H. Moon, S. C. Park, J. Jang, Y. S. Kang, *Mater. Lett.* **2019**, *242*, 191.
- [29] X. Jiang, X. Fu, D. Ju, S. Yang, Z. Chen, X. Tao, *ACS Energy Lett.* **2020**, *5*, 1797.
- [30] J. Ávila, C. Momblona, P. P. Boix, M. Sessolo, H. J. Bolink, *Joule* **2017**, *1*, 431.
- [31] E. Climent-Pascual, B. C. Hames, J. S. Moreno-Ramírez, A. L. Álvarez, E. J. Juárez-Perez, E. Mas-Marza, I. Mora-Seró, A. De Andrés, C. Coya, *J. Mater. Chem. A* **2016**, *4*, 18153.
- [32] E. S. Parrott, J. B. Patel, A. A. Haghghirad, H. J. Snaith, M. B. Johnston, L. M. Herz, *Nanoscale* **2019**, *11*, 14276.
- [33] G. Grancini, S. Marras, M. Prato, C. Giannini, C. Quarti, F. De Angelis, M. De Bastiani, G. E. Eperon, H. J. Snaith, L. Manna, A. Petrozza, *J. Phys. Chem. Lett.* **2014**, *5*, 3836.

- [34] V. D'Innocenzo, A. R. S. Kandada, M. De Bastiani, M. Gandini, A. Petrozza, A. R. Srimath Kandada, M. De Bastiani, M. Gandini, A. Petrozza, *J. Am. Chem. Soc.* **2014**, *136*, 17730.
- [35] L. Zhang, W. Geng, C. J. Tong, X. Chen, T. Cao, M. Chen, *Sci. Rep.* **2018**, *8*, 1.
- [36] A. Babaei, K. P. S. Zanoni, L. Gil-Escrig, D. Pérez-del-Rey, P. P. Boix, M. Sessolo, H. J. Bolink, *Front. Chem.* **2020**, *7*, 1.
- [37] A. Babaei, C. Dreessen, M. Sessolo, H. J. Bolink, *RSC Adv.* **2020**, *10*, 6640.
- [38] G. Grancini, A. R. Srimath Kandada, J. M. Frost, A. J. Barker, M. De Bastiani, M. Gandini, S. Marras, G. Lanzani, A. Walsh, A. Petrozza, *Nat. Photonics* **2015**, *9*, 695.
- [39] L. Oesinghaus, J. Schlipf, N. Giesbrecht, L. Song, Y. Hu, T. Bein, P. Docampo, P. Müller-Buschbaum, *Adv. Mater. Interfaces* **2016**, *3*, 1.
- [40] M. L. Herrera, R. W. Hartel, *J. Am. Oil Chem. Soc.* **2000**, *77*, 1177.
- [41] P. Schulz, L. L. Whittaker-Brooks, B. A. Macleod, D. C. Olson, Y. L. Loo, A. Kahn, *Adv. Mater. Interfaces* **2015**, *2*, 1.
- [42] E. M. Miller, Y. Zhao, C. C. Mercado, S. K. Saha, J. M. Luther, K. Zhu, V. Stevanović, C. L. Perkins, J. Van De Lagemaat, *Phys. Chem. Chem. Phys.* **2014**, *16*, 22122.
- [43] S. Chen, T. W. Goh, D. Sabba, J. Chua, N. Mathews, C. H. A. Huan, T. C. Sum, *APL Mater.* **2014**, *2*, 1.
- [44] D. Kim, J. H. Yun, M. Lyu, J. Kim, S. Lim, J. S. Yun, L. Wang, J. Seidel, *J. Phys. Chem. C* **2019**, *123*, 14144.
- [45] A. A. Zhumekenov, M. I. Saidaminov, M. A. Haque, E. Alarousu, S. P. Sarmah, B. Murali, I. Dursun, X. H. Miao, A. L. Abdelhady, T. Wu, O. F. Mohammed, O. M. Bakr, *ACS Energy Lett.* **2016**, *1*, 32.
- [46] E. Alarousu, A. M. El-Zohry, J. Yin, A. A. Zhumekenov, C. Yang, E. Alhabshi, I. Gereige, A. Alsaggaf, A. V. Malko, O. M. Bakr, O. F. Mohammed, *J. Phys. Chem. Lett.* **2017**, *8*, 4386.
- [47] K. Wang, D. Yang, C. Wu, J. Shapter, S. Priya, *Joule* **2019**, *3*, 311.
- [48] S. D. Stranks, *ACS Energy Lett.* **2017**, *2*, 1515.